Materials Science and Engineering A 412 (2005) 222–229

www.elsevier.com/locate/msea

3D analysis of creep voids in hydrogen reformer tubes

Azmi Abdul Wahab, Milo V. Kral *

Department of Mechanical Engineering, University of Canterbury, Private Bag 4800, Christchurch, New Zealand

Accepted 18 August 2005

Abstract

An ex-service hydrogen reformer tube composed of Fe–0.45% C–25% Cr–35% Ni–1.0% Si–1.5% Nb–1.0% Mn (approximate wt.%) was examined via serial sectioning and 3D reconstruction to characterize creep voids in terms of their size, location, and surrounding precipitates. In addition, electron backscatter diffraction (EBSD) technique was used to investigate any crystallographic influence on the location of these voids. Observations in 3D show that void distribution is not uniform in terms of size, shape, and location. Most of the voids are oblong and occur at grain edges and corners. In addition, all observed voids were in contact with the Cr-rich $M_{23}C_6$ precipitates. EBSD results showed that 80% of the $M_{23}C_6$ precipitates surrounding these voids have an irrational crystallographic orientation relationship (OR) with the austenite matrix, contrary to the expectation that grain boundary precipitates nearly always obtain rational OR with respect to one adjacent grain.

Keywords: 3D reconstruction; Creep voids; Reformer tube; EBSD; Orientation relationship

1. Introduction

In petrochemical plants, the production of hydrogen from natural gas is carried out in hydrogen reformers where the following reactions occur in the presence of a nickel catalyst:

$$CH_4 + H_2O \rightarrow CO + 3H_2$$

$$CO + H_2O \rightarrow CO_2 + H_2$$

Hydrogen reformers consist of hundreds of vertically oriented catalyst-filled tubes operating at a temperature of more than 900 °C and an internal pressure of approximately 2 MPa. These tubes have an internal diameter and wall thickness of about 125 and 10 mm, respectively, and are typically expected to sustain service for 100,000 h (11.4 years) with diametral strain not exceeding 3%. These service requirements result in high temperature deformation in a regime of relatively low stresses (less than 20 MPa), and low creep rates ($8 \times 10^{-11}\ s^{-1}$) where the reported creep mechanisms are diffusional creep, Harper-Dorn (H-D) creep, and grain boundary sliding [1,2].

Centrifugally cast austenitic stainless steel alloys containing high amounts of carbon (0.4 wt.%), chromium (25 wt.%) and nickel (20–35 wt.%) were developed for these purposes. The additions of Cr and Ni are well known for improving corrosion resistance and strength at elevated temperatures, while the high amount of C inhibits σ-phase formation [3]. Creep strengthening is achieved via the formation of Cr-rich $M_{23}C_6$ carbides in the reformer tube microstructure. Primary carbides, which form a grain boundary network during casting, are suspected to play an important role in restraining grain boundary sliding [4]. The secondary carbides, which appear as fine intragranular precipitates during service, are believed to hinder dislocation motion [4]. With increasing service time, the primary and secondary Cr-rich $M_{23}C_6$ carbide particles have a tendency to coarsening, which in turn reduces creep strength [5]. Additions of Nb and Ti lead to "fragmentation" and refinement of the grain boundary carbide network, as well as creating a finer and more stable dispersion of intergranular carbides, which would all result in added creep resistance [6–8].

It is well known from previous work on austenitic stainless steels [9–14] that $M_{23}C_6$ nucleation site has an influence on the crystallography of these precipitates. For instance, $M_{23}C_6$ precipitation in the grain interior results in the best lattice match (cube-cube OR), while grain boundary carbides obtain a near-rational OR with at least one adjacent austenite grain [10]. This is significant because material behaviour appeared to be linked to crystallographic relationship between the precipitate and the adjacent matrix. Corrosion studies on austenitic stainless steels by Kinzel [15] indicated that corrosion was more pronounced

* Corresponding author. Tel.: +64 3 3642987x7392; fax: +64 3 3642078.
E-mail address: milo.kral@canterbury.ac.nz (M.V. Kral).

0921-5093/$ – see front matter © 2005 Elsevier B.V. All rights reserved.
doi:10.1016/j.msea.2005.08.223

Table 1
Main alloying elements (in wt.%) present in the reformer tube sample

C	0.49
Cr	23.5
Ni	32.1
Si	1.07
Nb	1.14
Ti	0.13
Mn	0.91
W	0.46
Fe + others	Bal

Remainder is Fe and other minor alloying elements.

on $M_{23}C_6$ interfaces having a low registry with the austenite matrix. More recent work on austenitic stainless steels under creep-fatigue conditions show that higher coherency of grain boundary $M_{23}C_6$ carbides result in better resistance to cavity nucleation [16].

Three-dimensional analysis of microstructures is often very useful in understanding true microstructural features of materials [17,18]. Earlier attempts in 3D analysis usually involved a serial sectioning technique and motion pictures [19] or some form of physical reconstruction method [20] to provide a representation of the features in 3D. With the advent of superior image processing and visualization software and the corresponding computer hardware, 3D analysis of microstructures have been successfully employed in understanding microstructural characteristics in materials such as alloy steels [21] and particle reinforced metal matrix composites [22].

In the present work, an ex-service hydrogen reformer tube was examined via serial sectioning and computer-aided 3D reconstruction. The serial sectioning and 3D reconstruction techniques revealed the shapes, sizes, locations, and adjacent precipitates of the creep voids in 3D, information that cannot be obtained from two-dimensional micrographs alone. Additionally, crystallographic orientations of the phases adjacent to creep voids were obtained by electron backscatter diffraction (EBSD) to determine any crystallographic trends in creep void locations. It is anticipated that 3D data obtained from this and additional work will be applied to various available creep failure models [23,24].

2. Experimental details

The ex-service hydrogen reformer tube obtained for this work has been in service at approximately 940 °C and 2 MPa internal pressure for 60,000 h (6.8 years). Chemical composition for this tube is listed in Table 1. A sample from the reformer tube was mounted in Buehler Epomet epoxy, and underwent grinding and polishing steps of 240 and 400 grit silicon carbide papers, 9 and 3 μm diamond paste, culminating with a final polish of 0.06 μm colloidal silica. A "control" sample was also prepared from an as-cast tube made from the same alloy as the ex-service tube. This sample was aged at 1030 °C for 500 h in air, and will be used to compare the crystallography of the precipitates. For reference, the Larson-Miller parameter for the control sample is 33.4 compared to a value of 33.6 for the ex-service sample.

For optical microscopy (OM) examinations, the samples were etched in glyceregia (10 ml glycerol + 15 ml HCl + 5 ml HNO_3) prior to observation using a Leica DM-IRM Microscope with Zeiss Axiocam digital camera. For scanning electron microscopy (SEM), energy dispersive spectroscopy (EDS), and electron backscatter diffraction (EBSD), the samples were examined after an extended polish in colloidal silica. The equipment employed for SEM, EDS and EBSD examinations are JEOL JSM-6100 scanning electron microscope, Oxford eXL energy dispersive analyzer with a Be window, and HKL Technology EBSD system. An accelerating voltage of 20 kV was utilized for these observations.

X-ray diffraction (XRD) was also used to confirm the precipitates present in the material. A small sample of the tube was immersed in glyceregia for up to 8 h (successive immersions of two hours per fresh solution) to dissolve the austenite matrix. The remaining precipitate was powdered and scanned in a Philips PW1729 XRD system at 50 kV and 40 mA Cu Kα radiation. Identification of peaks was performed by matching simulated patterns of various compounds generated from Pearson's Handbook [25].

Transmission electron microscopy (TEM) was used to characterize fine intragranular precipitates present in the material. TEM samples were initially thinned in a solution of 35% *n*-butyl alcohol, 6% perchloric acid, and 59% methanol at −30 °C, 40 V, and 25 mA using an E.A. Fischione twin-jet electropolishing setup followed by ion milling using a Gatan Precision Ion Polishing System. TEM examination was performed using a Hitachi H600 transmission electron microscope at 100 kV.

In general, the serial sectioning technique employed here is similar to previous work [21]. Serial sectioning was performed only on the ex-service tube, which was done by successive polishing of the sample using 1 μm diamond compound and 0.06 μm colloidal silica suspension. Prior to the serial sectioning process, reference fiducial marks were placed on the sample using a Leco microhardness tester in order to identify areas of interest and also to align the image stacks for later 3D reconstruction. Furthermore, size reduction of the fiducial marks indicated the amount of material removed with each section. Before the marks were completely polished off, new marks were made so that continuity was preserved for the next polishing steps. Serial sections were done at 0.5 μm steps for sixty five layers (32 μm). Prior to imaging, the sample was lightly etched in glyceregia. A total of four areas of the sample were selected for study; two 400 μm × 300 μm areas and two 160 μm × 120 μm areas were imaged at original magnifications of 200× and 500×, respectively. Due to the relatively large size of the grains involved (in excess of 150 μm), it was ascertained that only the two 400 μm × 300 μm areas were suitable for 3D reconstruction and analysis.

After layers 45, 55 and 65, all four areas of interests in the sample were subjected to EBSD scans to generate an overall orientation map. Following the EBSD mapping, the voids and their immediate surroundings were imaged using forescatter Z-contrast (FZ) and forescatter orientation (FO) detectors, in addition to the usual secondary electron (SE) image. The forescatter Z-contrast detector revealed atomic number contrast

of the different phases present while the forescatter orientation contrast detector exposed grains or subgrains within the matrix and precipitates.

EBSD patterns (or EBSPs) were then recorded in spot mode for specific locations of the matrix and precipitates surrounding the creep voids. For each carbide grain in contact with a creep void, EBSPs were obtained from the carbide as well as the austenite grains on both sides of the grain boundary. In instances where the carbide grain contains subgrains, EBSPs were obtained from each subgrain if its size is larger than the size of the electron beam. The occurrence of these subgrains within larger carbide colonies would certainly influence the OR data obtained if the electron beam size is larger than the subgrain size. EBSD scans were also carried out on the "control" sample. Since the control sample did not contain any creep voids, grain boundary precipitates were selected at random and EBSPs were obtained for these precipitates and the adjacent austenite matrices. HKL Technology's Flamenco software was used to analyse the EBSPs, which then automatically calculated a 3×3 orientation matrix for each EBSP. The misorientation M between any two phases (A and B) can then be obtained from the matrix operation:

$$[\mathrm{A}][\mathrm{B}] - 1 = [\mathrm{M}]$$

where [A] and [B] are orientation matrices of locations within phases A and B with respect to an arbitrary reference axis system. Assuming that:

$$[\mathrm{M}] = \begin{bmatrix} m_{11} & m_{12} & m_{13} \\ m_{21} & m_{22} & m_{23} \\ m_{31} & m_{32} & m_{33} \end{bmatrix}$$

the orientation relationship (OR) between location A and B is then:

$$[m_{11} \quad m_{21} \quad m_{31}]_{\mathrm{A}} // [1 \quad 0 \quad 0]_{\mathrm{B}}$$
$$[m_{12} \quad m_{22} \quad m_{23}]_{\mathrm{A}} // [0 \quad 1 \quad 0]_{\mathrm{B}}$$
$$[m_{31} \quad m_{32} \quad m_{33}]_{\mathrm{A}} // [0 \quad 0 \quad 1]_{\mathrm{B}}$$

The misorientation angle θ and axis $[u\ v\ w]$ between A and B can also be calculated from misorientation matrix [M] by the following equations:

$$\theta = \cos^{-1}\left(\frac{m_{11} + m_{22} + m_{33} - 1}{2}\right)$$

$$[u \quad v \quad w] = [m_{23} - m_{32} \quad m_{31} - m_{13} \quad m_{12} - m_{21}]$$

Micrographs of serial sections were first aligned based on the fiducial marks. For this purpose, the public-domain NIH ImageJ 1.3 [26] software was employed. This software has available software "plug-ins" specific for aligning image stacks from serial sections as well as the ability to generate crude 3D renditions and animations for quick checking of the sectioned volume to reveal creep voids and their surroundings. After image alignment, specific features in individual serial section images were identified and a separate image stack was created for the series of images containing similar features. For instance, all creep voids were highlighted (with other areas blacked out) in each serial section image and an image stack containing only voids were created. The same treatment was performed to highlight different precipitates present and then each of these features was stored in their respective image stack. From the individual image stacks, information such as void volume or carbide volume fraction can be determined by counting voxels (volume picture elements), which were then converted into units of volume. For 3D reconstruction, a computer program was written using RSI's IDL 6.0 [27] to read the image stacks, and interpolate between image layers to produce a three-dimensional representation of the volume. This 3D representation can be rotated about any axis and animated for further study. By loading the specific image stacks, microstructural features can be revealed or hidden as needed. Specific colors were attributed to various microstructural features for enhanced visualization.

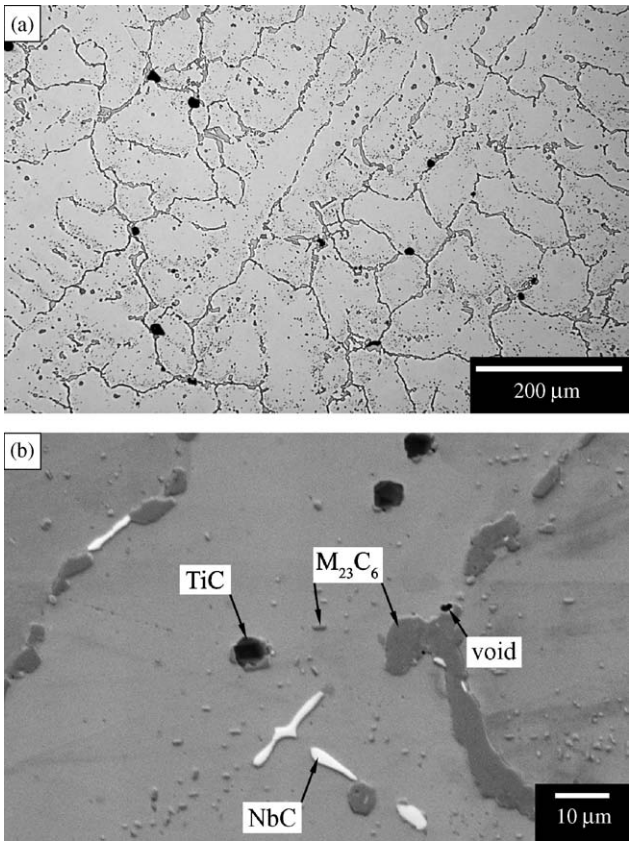

Fig. 1. Microstructure of ex-service reformer tube; (a) optical microscope image of sample etched in glyceregia; (b) backscatter electron (BSE) image identifying three precipitate types $M_{23}C_6$, NbC, and TiC.

3. Results and discussion

Fig. 1a shows the general appearance of the microstructure of the ex-service tube, while Fig. 1b is a backscatter electron (BSE) image of the tube with the various types of precipitates labelled. Identification of coarse precipitates was performed by a combination of EDS, EBSD and XRD, as described previously. Identification of fine precipitates was achieved via TEM and SAD. There were three types of precipitates present in the material:

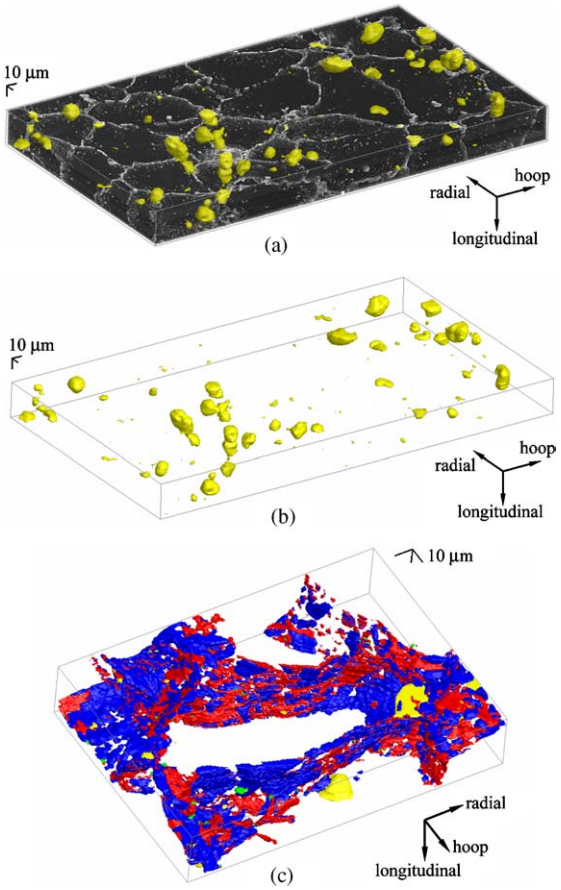

Fig. 2. 3D reconstruction of a 403 μm × 204 μm × 32 μm volume; (a) reconstruction with austenite shown in black, voids in yellow, and precipitates shown in shades of grey; (b) reconstruction of 138 voids; (c) reconstruction a 130 μm × 179 μm × 32 μm sub-volume showing voids (yellow), $M_{23}C_6$ (blue), NbC (red) and TiC (green).

- Cr-rich $M_{23}C_6$—appeared both intragranularly as fine precipitates and along the grain boundaries as coarse intergranular precipitates;
- NbC—found along the grain boundaries;
- TiC—predominantly occurred intragranularly.

Characterization of the "control" sample revealed that the same three precipitate types were also present.

Fig. 2 displays the isometric views of 3D reconstructions of one of the sectioned volume. In Fig. 2a, a total of 138 creep voids are reconstructed and highlighted in yellow and are superimposed on the 3D volume. Fig. 2b and c show only the voids and grain-boundary precipitates, respectively. The first observation made from these 3D reconstructions is that the creep voids are not uniformly distributed in the sample volume in terms of size, shape, and location. This observation highlights the importance of 3D techniques to reveal the true microstructure of materials. For this study, the 3D analysis outputs were void size, shape, location, and contact precipitate(s). Void sizes are represented by the equivalent sphere diameters of the void volumes. This was done to give a linear dimension value (i.e. μm), which conveniently represents the void size. For instance, it would be easier to visualize a 10 μm diameter void than the same void with a volume of 524 μm^3. Void shape was classified into three types—spherical, peanut, and ellipsoidal, as shown in Fig. 3. Spherical voids are approximately equiaxed, peanut-shape voids appear to be a coalescence of two or more spherical voids, and ellipsoidal voids are elongated-shaped voids without a distinct waist as seen in peanut-shaped voids. Void locations are shown schematically in Fig. 4 and categorized as follows:

- boundary—void located at boundary plane between two austenite grains;
- edge—void located at intersecting edge of three austenite grains;
- corner—void located at the intersecting corner of four (or more) austenite grains.

"Contact precipitates" were determined by viewing the 3D reconstruction to determine which precipitates are in contact with the voids.

A total of 290 voids were reconstructed from two serial-sectioned volumes, and their various characteristics observed from the 3D reconstruction are summarized in Fig. 5. Fig. 5a shows the overall void distribution represented by the equivalent void diameter. Total void volume for each diameter classification is indicated on the left axis while the number of voids in each class is indicated on the right axis. This graph simply points out that although there are a higher number of voids with diameters less than 4 μm, the total volume occupied by these voids is small compared to the total volume occupied by voids that are larger than 12 μm diameter. Fig. 5b shows a further breakdown of the void distribution in terms of their location within the grain structure. The larger voids appear predominantly along

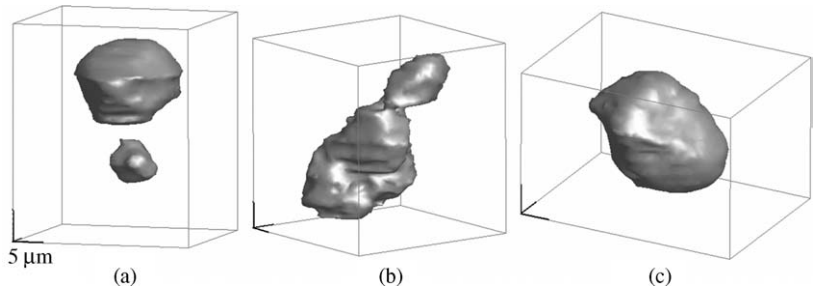

Fig. 3. Classification of creep void shapes; (a) spherical voids; (b) peanut-shaped void which appear to be a joining together of two or more voids; (c) ellipsoidal void.

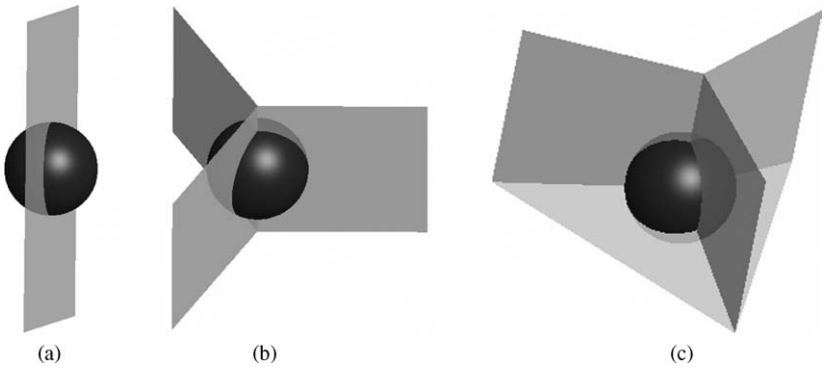

Fig. 4. Schematic representations of void location classification; (a) void located on the boundary plane between two grains; (b) void situated at the intersecting edge of three grains; (c) void located at the intersecting corner of four grains.

grain edges and corners (intersection of three and four grains, respectively), while smaller voids are located primarily along boundaries (between two grains) and edges. There were a few instances of voids appearing intragranularly (within austenite grains) where they appear adjacent to Cr-rich $M_{23}C_6$ precipitates. These void locations are categorized as "Intragranular" on Fig. 5b, and due to the low frequency of occurrence, their appearance on the graph is hardly visible.

Fig. 5c displays the correlation between void location and void shape. Peanut-shaped voids account for most of the total void volume, perhaps unsurprisingly, since this void type appears to be a coalescence of two or more voids. Ellipsoidal voids occupy the least amount of space, but it can be argued that these voids might also be a coalescence of two voids. In terms of numbers, there were more voids occurring at boundaries between two grains, however, the total volume of the voids at this location is less than as tenth of the volume taken up by voids at grain edges and corners. A possible explanation would be that creep voids are most likely to nucleate first at grain edges and corners where there would be more vacancies due to lattice mismatch between carbide and austenite. Moreover, the occurrence of large voids at these locations are consistent with the

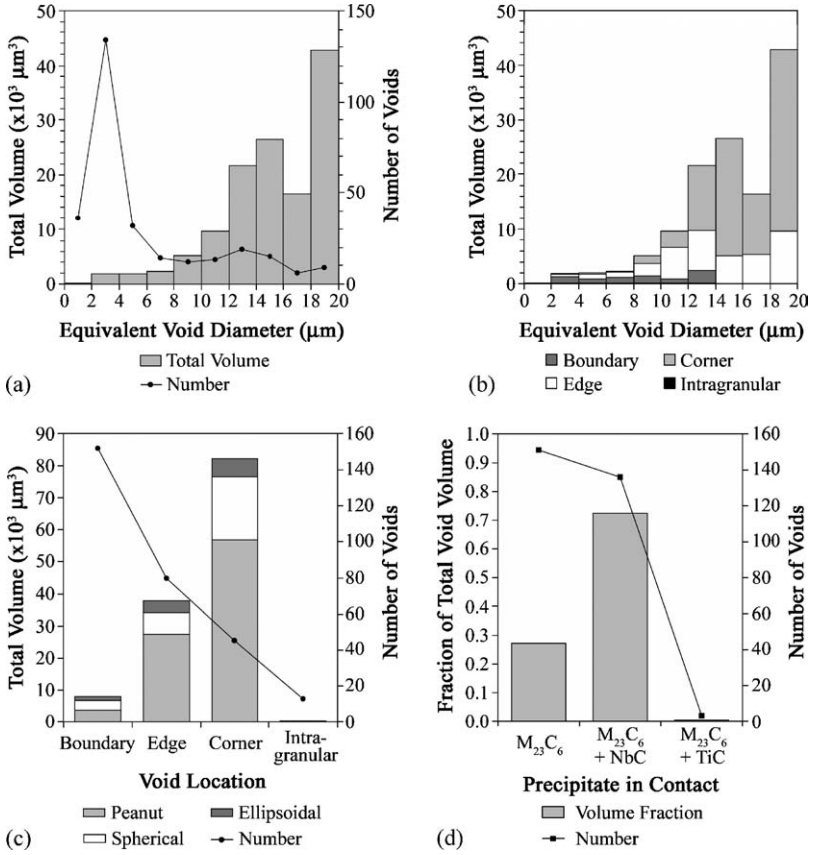

Fig. 5. Characteristics of creep void obtained from 3D reconstruction of reformer tube material. Total number of voids analyzed is 290 obtained from two reconstructed volumes; (a) overall distribution of total void volume and number for various sizes of voids; (b) distribution in (a) is further categorized in terms of void location; (c) correlation between void location and void shape; (d) voids and contact precipitates listed as fraction of total void volume and void count.

current belief that void nucleation and growth transpires due to grain boundary sliding along geometrical irregularities at grain boundaries where stress concentration is high [28]. This would lead to more severe creep damage at grain edges and corners.

Fig. 5d displays the link between the precipitates in contact with the voids and their occurrences in terms number of voids and fraction of total void volume. Results show that a higher number of voids were in contact with only $M_{23}C_6$ precipitate but a higher fraction of total void volume came in contact with both $M_{23}C_6$ and NbC precipitates. The most significant observation made from Fig. 5d is that all the voids inspected came in contact with $M_{23}C_6$ somewhere along their perime-

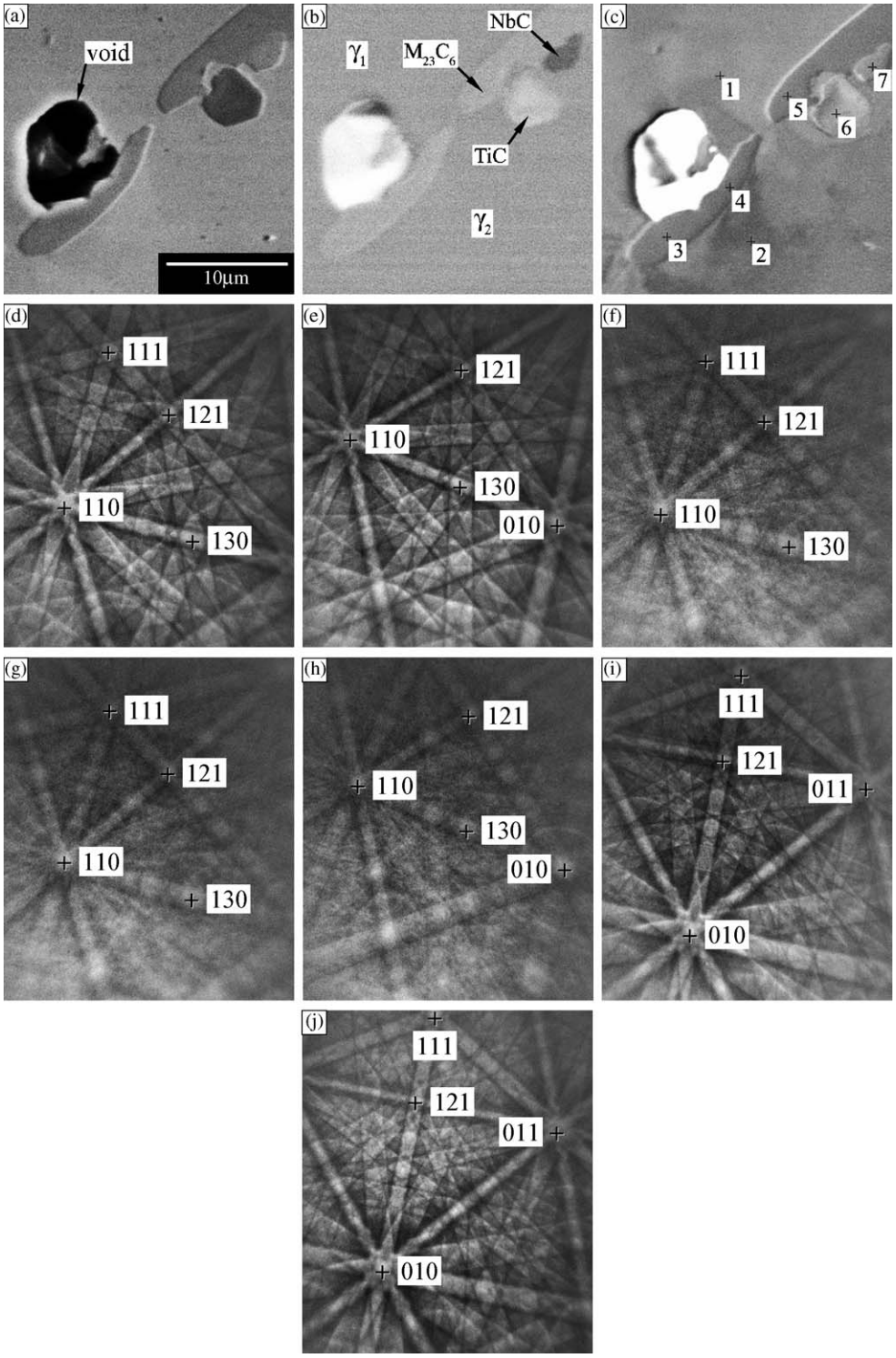

Fig. 6. (a) SE image of a creep void and surrounding area; (b) FZ image identifying various phases present; (c) FO image identifying the different grains and also specifying the locations where EBSPs were obtained; (d) EBSP of austenite (location 1); (e) EBSP of another austenite grain (location 2) (f–h) EBSPs of three $M_{23}C_6$ grains (locations 3, 4, 5); (i) EBSP of TiC (location 6); (j) EBSP of NbC (location 7).

ter. No voids were observed solely in contact with NbC and/or TiC precipitates. Correlation between creep void locations and $M_{23}C_6$ precipitates have been previously mentioned [28,29]. From the present inspection of a single ex-service tube, it cannot be conclusively said that these voids nucleated only at $M_{23}C_6$ precipitates. However, it should be noted that for the material volume inspected, there was twice the amount of $M_{23}C_6$ compared to NbC (approximately 7% versus 3%, by volume), and thus the absence of voids solely adjacent to NbC precipitates is conspicuous. Another comment to follow these observations is that there were no other types of inclusions or impurities found to be associated with the voids. One work on bainitic CrMoV steel has indicated that creep voids nucleate exclusively on grain boundary sulfides [30]. It has also been proposed that creep voids nucleate only on "nonadherent grain boundary inclusions" [28].

An example of the phase identification procedure is shown in Fig. 6. Fig. 6a–c are examples of SE, FZ, and FO images of a creep void and its vicinity. The locations where EBSPs were obtained are identified in Fig. 6c. Examples of typical EBSP's are shown in Fig. 6d–j. A combination of EDS and EBSD was used to identify the various precipitates observed.

Fig. 7a shows the OR between $M_{23}C_6$ precipitates adjacent to creep voids and each adjacent austenite matrix grain in the form of a [1 0 0] stereographic triangle. A total of 442 points was plotted. Data represented by filled squares are $M_{23}C_6$ precipitates with a near cube-cube OR (high registry) with an adjacent austenite grain while data represented by open squares are for $M_{23}C_6$ precipitates with a random OR. Typically an angular difference between grains of 10–15° is taken as low angle grain boundary, where dislocation arrays are able to compensate for the interface mismatch [31]. For this work, near cube-cube OR is based on a misorientation angle of 10° or less. Fig. 7b shows the distribution of misorientation angles for $M_{23}C_6$ precipitates and austenite grains in the vicinity of the creep voids. The distribution showed that approximately twenty percent of the $M_{23}C_6$ precipitates adjacent to voids show a near cube-cube OR.

Previous work by King and Bell [32] stated that grain boundary precipitates should obtain rational OR with one of the adjacent grains. Additionally, works by Lewis and Hattersley [9] and Beckitt and Clark [11] on $M_{23}C_6$ precipitates in austenitic stainless steels have also indicated that grain boundary $M_{23}C_6$ precipitates should display a cube-cube OR with at least one of the adjacent austenite grains. Furthermore, long term ageing such as the service condition experienced by the ex-service reformer tube would typically result in coalescing of the grain boundary carbides towards a near cube-cube OR so that the total surface energy is lowered [9]. This would imply that the occurrence of cube-cube OR between $M_{23}C_6$ precipitates and the adjacent austenite grains should be 50%. Interestingly, this hypothesis was demonstrated by the "control" sample, which underwent high temperature ageing. The OR data for the control sample (total of 272 points) showed a less random appearance,

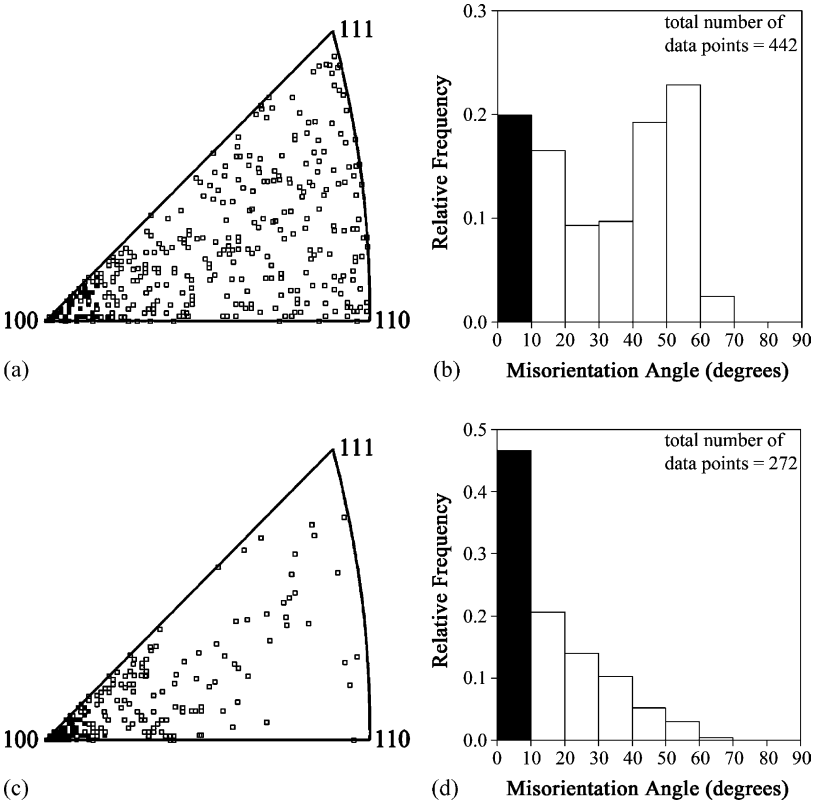

Fig. 7. Comparison of orientation relationships and misorientation angles between ex-service material and laboratory-aged sample; (a) OR between $M_{23}C_6$ and austenite grains in ex-service tube sample, closed squares indicate $M_{23}C_6$ precipitates with near cube-cube OR with austenite; (b) misorientation angle distribution of OR data shown in (a), black histogram bar correspond to near cube-cube data; (c) OR between $M_{23}C_6$ and austenite grains in laboratory-aged sample; (d) misorientation angle distribution of OR data shown in (c).

as indicated in Fig. 7c, while the misorientation angle distribution in Fig. 7d established that cube-cube OR between $M_{23}C_6$ precipitates and austenite occurred forty seven percent of the time. It is important to recall that the Larson-Miller parameters for both the ex-service sample and the "control" sample are similar (33.6 and 33.4, respectively). Based on these observations, it is believed that the twenty percent occurrence of $M_{23}C_6$ with cube-cube OR near creep voids occurs because the preferred sites for creep voids are low registry boundaries between $M_{23}C_6$ precipitates and austenite.

4. Conclusions

Creep voids in an ex-service hydrogen reformer tube have been studied via serial sectioning and 3D reconstruction. Creep voids are not uniformly distributed through the volume in terms of their size, shape, and location. The largest voids were formed by coalescence of two or more voids resulting in a peanut shape. Almost all of the voids appeared near grain boundary carbides and the larger of these voids were located at grain edges and corners. All voids made contact with $M_{23}C_6$ precipitates, whereas no voids were observed in sole contact with TiC or NbC precipitates. EBSD observation of the $M_{23}C_6$ precipitates surrounding these voids showed that most of the voids are adjacent to precipitates with a random OR with the surrounding austenite matrix.

Acknowledgements

The authors would like to thank Methanex (NZ) Ltd. and Schmidt & Clemens (Spain) for funding of this work.

References

[1] T.G. Langdon, Metall. Mater. Trans. 33A (2002) 249–259.
[2] F.R.N. Nabarro, Metall. Mater. Trans. 33A (2002) 213–218.
[3] T. Sourmail, Mater. Sci. Technol. 17 (2001) 1–14.
[4] G.D. Barbabela, L.H. de Almeida, T.L. da Silveira, I. Le May, Mater. Characterization 26 (1991) 1–7.
[5] G.D. Barbabela, L.H. de Almeida, T.L. da Silveira, I. Le May, Mater. Characterization 26 (1991) 193–197.
[6] L.H. de Almeida, A.F. Ribeiro, I. Le May, Mater. Characterization 49 (2003) 219–229.
[7] T. Shinoda, M.B. Zaghloul, Y. Kondo, R. Tanaka, Trans. ISIJ 18 (1978) 139–148.
[8] H. Wen-Tai, R.W.K. Honeycombe, Mater. Sci. Technol. 1 (1985) 390–397.
[9] M.H. Lewis, B. Hattersley, Acta Metall. 13 (1965) 1159–1168.
[10] U.E. Wolff, Trans. Metall. Soc. AIME 236 (1966) 19–27.
[11] F.R. Beckitt, B.R. Clarck, Acta Metall. 15 (1967) 113–129.
[12] L.K. Singhal, J.W. Martin, Trans Metall Soc AIME 242 (1967) 814–819.
[13] L.K. Singhal, J.W. Martin, Acta Metall. 15 (1967) 1603–1610.
[14] P.H. Pumphrey, J.W. Edington, Acta Metall. 22 (1974) 89–94.
[15] A.B. Kinzel, Trans. AIME 194 (1952) 469–488.
[16] K.J. Kim, H.U. Hong, K.S. Min, S.W. Nam, Mater. Sci. Eng. A387–389 (2004) 531–535.
[17] M.V. Kral, M.A. Mangan, G. Spanos, R.O. Rosenberg, Mater. Characterization 45 (2000) 17–23.
[18] M.V. Kral, G. Ice, M.K. Miller, M.D. Uchic, R.O. Rosenberg, in: G.V. Voort (Ed.), ASM International Metallography and Microstructures Handbook, Vol. 9, ASM International, Materials Park, Ohio, 2004, pp. 448–467.
[19] M. Hillert, in: V.F. Zackay, H.I. Aaronson (Eds.), The Decomposition of Austenite by Diffusional Processes, Interscience, New York, 1962, pp. 197–237.
[20] O. Forsman, Jernkontor-ets Ann. 102 (1918) 1–30.
[21] M.V. Kral, G. Spanos, Acta Mater. 47 (1999) 711–724.
[22] M. Li, S. Ghosh, T.N. Rouns, H. Weiland, O. Richmond, W. Hunt, Mater. Characterization 41 (1998) 81–95.
[23] R. Raj, M.F. Ashby, Acta Metall. 23 (1975) 653–666.
[24] M.E. Kessner, T.A. Hayes, Int. J. Plasticity 19 (2003) 1715–1748.
[25] P. Villars, L.D. Calvert, Pearson's Handbook of Crystallographic Data for Intermetallic Phases, Second ed., ASM International, Materials Park, Ohio, 1991.
[26] NIH, http://rsb.info.nih.gov/ij/.
[27] RSI, http://www.rsinc.com/.
[28] V. Sklenicka, K. Kucharova, M. Svoboda, L. Kloc, J. Bursik, A. Kroupa, Mater. Characterization 51 (2003) 35–48.
[29] G. Muralidharan, P.J. Maziasz, N.D. Evans, M.L. Santella, K.C. Liu, J.G. Hemrick, V.K. Sikka, R.I. Pankiw, in MS&T. 2004. New Orleans, Lousiana.
[30] B.J. Cane, C.J. Middleton, Metal Sci. 15 (1981) 295.
[31] V. Randle, The Measurement of Grain Boundary Geometry, Electron Microscopy, in: B. Cantor, M.J. Goringe (Eds.), Materials Science Series, Institute of Physics Publishing, Bristol, 1993.
[32] A.D. King, T. Bell, Metall. Trans. 6 (1975) 1419–1429.